Title

Understanding the Mechanism of Electronic Defect Suppression Enabled by Nonidealities in Atomic Layer Deposition

Journal

Journal of the American Chemical Society, 142(1)

ISSN

0002-7863

Authors

Kavrik, Mahmut Sami

Bostwick, Aaron

Rotenberg, Eli

et al.

Publication Date

2020-01-08

DOI

10.1021/jacs.9b06640

Peer reviewed

Understanding the Mechanism of Electronic Defects Suppression Enabled by Non-Idealities in Atomic Layer Deposition

Mahmut Sami Kavrik[1], Aaron Bostwick[2], Eli Rotenberg[2], Kechao Tang[3], Emily Thomson[1], Toshihiro Aoki[4], Bernd Fruhberger[5], Yuan Taur[1], Paul C. McIntyre[3] and Andrew C. Kummel[1]

[1]Materials Science and Engineering, University of California San Diego, La Jolla, California, 92093

[2]Advanced Light Source (ALS), E. O. Lawrence Berkeley Laboratory, Berkeley, CA, USA

[3]Materials Science and Engineering, Stanford University, Stanford, California, 94305

[4]Irvine Materials Research Institute, University of California Irvine, Irvine, CA, USA

[5]California Institute for Telecommunications and Information Technology, University of California San Diego, La Jolla, CA 92093, United States

Corresponding author: Andrew Kummel, akummel@ucsd.edu

Abstract

Silicon germanium (SiGe) is a multi-functional material considered for quantum computing, neuromorphic devices and CMOS transistors. However, implementation of SiGe in nano-scale electronic devices necessitates suppression of surface states dominating on electronic properties. The absence of a stable and passive surface oxide for SiGe results formation of charge traps at the SiGe - oxide interface induced by GeO_x. In an ideal ALD process in which oxide is grown layer-by-layer, the GeO_x formation should be prevented with selective surface oxidation (i.e. formation of an SiO_x interface) by controlling oxidant dose in first few ALD cycles of the oxide deposition on SiGe. However, in a real ALD process,

the interface evolves during entire ALD oxide deposition due to diffusion of reactant species through the gate oxide. In this work, this diffusion process in non-ideal ALD is investigated and exploited: the diffusion through the oxide during ALD is utilized to passivate the interfacial defects by employing ozone as a secondary oxidant. Periodic ozone exposure during gate oxide ALD on SiGe is shown to reduce the integrated trap density (D_{it}) across the band gap by nearly an order of magnitude in Al_2O_3 ($< 6\times10^{10}$ cm^{-2}) and in HfO_2 ($< 3.9\times10^{11}$ cm^{-2}) by forming a SiO_x rich interface on SiGe. Depletion of Ge from the interfacial layer (IL) by enhancement of volatile GeO_x formation and consequent desorption from the SiGe with ozone insertion during ALD growth process is confirmed by electron energy loss spectroscopy (STEM-EELS) and hypothesized to be the mechanism for reduction of the interfacial defects. In this work, the nanoscale mechanism for defect suppression at SiGe oxide interface is demonstrated which is engineering of diffusion species in ALD process due to facile diffusion of reactant species in non-ideal ALD.

Introduction

Silicon Germanium (SiGe) is promising material system for novel electronic devices due to quantum confinement thanks to mature scaling technology. It is being investigated for (i) quantum computing due to its long spin coherence time[2-4], (ii) neuromorphic devices due to threading dislocations allowing controlled filament formation for resistive switching[6] and (iii) for channels in p-type metal oxide semiconductor (p-MOS) for boosting transistor performance due to high carrier mobility[7-9]. High transconductance in SiGe channels was reported by Hashemi et al via replacement high k/metal gate or interlayer oxides[10-11]. While SiGe transistors with high-k dielectrics are being actively developed for commercial high speed, low power electronic devices; the practical integration of SiGe as a top surface channel in complementary metal oxide semiconductor (CMOS) transistors is hindered by poor interface formation between the gate oxide and SiGe primarily due to GeO_x formation[12-13]. Elimination of unstable GeO_x species may be possible with Si cap layers epitaxially grown on SiGe channels for planar devices;

however it may be problematic for gate-all-around devices or FinFETs due to space constraints and the limitation in Si ALDs which may have low mobility due to defects[14]. Previous studies on defect suppression at the gate oxide-SiGe interface have included pre ALD passivation with nitrides[15-16] and sulfur[17] and post ALD selective oxygen scavenging with physical vapor deposited (PVD) gettering metal gates[12, 18]. However, the interfaces are still degraded mainly by Ge out-diffusion[13] during ALD at elevated temperatures. There are also processing challenges, for example the gettering metal inducing a reduction in maximum capacitance by forming thicker gate oxides and PVD being incompatible with nanoscale 3D devices employed[18]. Another approach for defect reduction is selective oxygen scavenging at high temperature (>500C). As shown by Lee at el. this technique utilizes the differences in bond strength between SiO_2 (3.48 eV) vs GeO_2 (2.82eV). The Ge-O bonds are broken selectively due to relative weakness compared to Si-O which causes selective Si oxidation with GeO out diffusion[19]. However, the thermal budget may be a concern for this process. Therefore, new approaches are needed for suppression of electronic defects in SiGe gate stacks.

Modification of semiconductor oxide interfaces during the ALD process using reactive oxygen species has been shown to be effective for reduction of charge traps via formation of GeO_2 (not GeO_x) interfaces on high Ge content Si substrates (>90%) by post oxidation through Al_2O_3 barrier using oxygen plasma as studied by Zhang et al[20], or ozone exposure reported by Ando et al., in which very high mobility was observed[21]. In these studies, instead of direct plasma oxygen or ozone dosing on SiGe surface, the Al_2O_3 was deposited prior to plasma oxygen or ozone dosing. However, it is seen that the ratio of Si to Ge in the substrate can greatly change the chemistry of post oxidation through Al_2O_3 barriers. For instance, it was reported that for pure Ge substrates, increasing the barrier Al_2O_3 thickness (1 to 1.5nm) prior to post-oxidation reduces the GeO_x IL thickness (from 1.2 to 0.23 nm) and unexpectedly increases D_{it} (~5×)[20]. For SiGe substrates, it was shown that post ALD oxidation on low Ge content SiGe (30% to 50%) forms a highly defective $SiGeO_x$ interface, and the thickness of the IL decreases for higher Ge

composition SiGe ($Si_{0.69}Ge_{0.31}$ to $Si_{0.5}Ge_{0.95}$) due to suppression of SiO_x in the IL[21]. However, DFT and experimental studies shown that formation of an SiO_x interface between SiGe and oxide results in an extremely low interfacial defect density on low Ge content SiGe[18].

In the present study, comprehensive analysis of the effect of reactive oxidant exposure during ALD oxide deposition is studied with impedance measurements correlated with STEM-EELS and photon energy dependent PES analysis to elucidate the defect reduction mechanism with ozone insertion. The impact of ozone exposure during ALD oxide deposition on the SiGe/high-k oxide interface is investigated with a large set of MOSCAP samples, including gate oxides of Al_2O_3 only, HfO_2 only, and hetero Al_2O_3-HfO_2 structures by comparing ozone exposure directly on SiGe or with Al_2O_3 and HfO_2 barriers. In contrast to previous reports on high Ge content SiGe[20-21], using ozone during HfO_2 gate oxide ALD on low Ge content SiGe ($Si_{0.7}Ge_{0.3}$) is found to decrease interface defects by reducing interfacial GeO_x. Ultra-low D_{it} of 0.32×10^{12} $cm^{-2}eV^{-1}$ is observed with very thin IL (<0.2nm) on $Si_{0.7}Ge_{0.3}$ with ozone insertion into ALD Al_2O_3 gate oxides. STEM-EELS analysis shows significant interface defect reduction with SiO_x rich IL formation with ozone exposure into ALD Al_2O_3 or HfO_2 gate oxide on $Si_{0.7}Ge_{0.3}$. PES revealed enhanced Ge and Si diffusion through HfO_2 during ALD growth with ozone insertion consistent with a low defect SiO_x rich interface formed by selective surface oxidation. The mechanism for defect suppression with ozone insertion into ALD oxide found to be different for Al_2O_3 and HfO_2. While ozone depletes Ge from the interface by forming GeO and enhances Ge out-diffusion depleting Ge from interface for both oxides, ultra-low D_{it} observed with ozone dosing during Al_2O_3 gate oxide ALD on SiGe is consistent with a second process occurring in which Al_2O_3 deposition selectively scavenges oxygen from the oxide/SiGe interface thereby further reducing defect density[5]. In this study, by correlating the two advance metrologies, STEM-EELS and energy-resolved PES, with multifrequency impedance spectroscopy, the mechanism for reduction of surface states during the ALD process is elucidated for the key new channel material in CMOS technology. However, a more general chemical insight is obtained. While ALD is

idealized as a layer-by-layer growth process, this is incorrect, but the non-idealities can be utilized for defect reduction. It is rare that non-idealities in semiconductor chemical processes actually improve the material quality.

Methods

Interfacial defects at the gate oxide/SiGe interface were analyzed and quantified with multifrequency impedance spectroscopy on MOSCAPs fabricated on 8 nm thick p-type $Si_{0.7}Ge_{0.3}$(100) epitaxially grown on p-type Si (100). Degreased SiGe substrates were cleaned with cyclic HF (aq), and sulfur passivated with $(NH_4)_2S$(aq). HfO_2 ($HfCl_4$ - 250ms, H_2O – 250ms) and Al_2O_3 (trimethyl aluminum (TMA – 500ms) – H_2O – 500ms) gate oxides were grown at 300C in a Beneq TFS200 ALD reactor. After optimization of the ozone pulse length, ozone was introduced during oxide ALD in a single pulse (60 sec with 100% power at a flow rate of 4 g/h (at 100 g/Nm^3, 20°C)) such as in Fig 1b, c, d or intermittently (5 sec each) (Fig. 1e "ozone nanolaminate - NL''). Gate metal and back contacts were formed with Ni thermal evaporation and Al sputtering. Optimized forming gas annealing (5%H_2/95%N_2) was employed in 3 steps 300C-330C-350C for 10 min each, details of the very similar MOSCAP fabrication process can be found elsewhere[18]. Electrical characterization of the MOSCAP devices was performed with a Keysight B1500 at 300 K by I-V and multifrequency C-V, G-V measurements from inversion at 2V to accumulation at -2V. Interface defects densities (D_{it}) at the oxide – SiGe interface were calculated with the full interface state model fitting capacitance and conductance graphs for each bias point[22-23]. As previously documented, multiple devices on the same wafer were probed to define standard D_{it} error analysis and verify the repeatability. It is shown that the typical standard error is 3.9%; therefore, relative D_{it} variation as low as 10% among different processing conditions can be reliably distinguished[5].

The structures and the compositions of the MOSCAP devices and interfaces were studied using electron transparent specimens (<50 nm) prepared from device cross sections with a FEI Scios Focused Ion Beam

using Ga ions and low energy Ar ions (<1keV) for the last step to remove the Ga beam damage. A JEOL JEM-ARM300F Transmission Electron Microscope equipped with double aberration correction was used in scanning transmission electron microscope (STEM) mode at 200keV both for imaging and compositional analysis. Oxide – semiconductor atomic structures were obtained by STEM high-angle annular dark field (HAADF) and bright field (BF) simultaneously. Similarly, the chemical composition of the devices was investigated simultaneously both with electron energy loss spectroscopy (EELS) and energy dispersive X-Ray spectroscopy (EDS) using a Gatan GIF Quantum ER and JEOL dual large-angle silicon-drift EDS detectors. Dual EELS including zero loss and core loss spectra were collected to correct the energy drift and deconvolute plural scattering. Gatan Digital Micrograph was used for the compositional analysis and multiple linear least square (MLLS) fitting was performed after background subtraction[24].

Surface and depth compositional profiles across the gate oxide were investigated with energy-resolved photoelectron spectroscopy (PES) using a nondestructive soft X-ray probe equipped with a Scienta R400 analyzer at the MAESTRO beamline (micro ARPES end station) at the Lawrence Berkeley National Lab Advanced Light Source (ALS). Since the depth profiling with ion sputtering can alter the local oxide composition, especially in HfO_2[25-26], depth composition profiling was studied with photon energy dependent PES. Photon energy dependent PES was chosen instead of angle dependent PES for depth profiling, since photon energy dependent PES can be done with a fixed experiment geometry and a small spot size; therefore, the composition of the oxide could be probed between the metal gates (Fig. 1)[27-28]. X-ray energy was varied between 150eV, 500eV and 1keV to benefit from differences in inelastic mean free path (λ) (IMFP) of the photoelectrons. It should be noted that the mean free path for elastically scattered photoelectrons can be longer than the IMFP (e.g. the elastic mean free path for photoelectrons at ~1keV in HfO_2 is ~6 nm[1]). In addition, even for inelastically scattered electrons, only 65% of the intensity originate within one x-ray wavelength λ of the top surface. Therefore, photon energy dependent PES

allowed probing the topmost layers due to the unique surface sensitivity obtained with low energy X-ray radiation as well as the oxide-SiGe interface probing with high energy X-rays with elastic and inelastic electrons.

The incident photons and detection angels have a fixed relationship defined by the spectrometer. The incident photons were at an angle of 54.75° with respect to the sample normal thereby positioning the electron spectrometer to measure at normal emission. The X-ray penetration depth is much deeper than the HfO_2 and SiGe layer thicknesses; therefore, the detection depth is mainly determined by the inelastic mean free path (λ) (IMFP) of the photoelectrons which is a function of the kinetic energy of the photo electrons; however, the effective distance through which the electrons travel through the sample is determined by the exit angle. Therefore, a normal detection angle was chosen since this is shortest path for photoelectrons to exit the substrate.

The soft X-ray photons were focused onto samples with a beam cross section of 40 x 40 μm^2 located on the HfO_2 surface between the Ni gate metals of the MOSCAP devices as shown in Fig 1. Each sample was probed at six points with 10 scans averaged at each point. Compositions of the oxide at selected energy-depth were obtained by monitoring Ge 3d, Hf 4f and Si 2p core level lines at narrow energy scan. Since the focus of the experiments is Si and Ge composition in the HfO_2 and at the interface, the constant kinetic energy PES method[28] was employed by choosing the close ionization edges of Hf $4f_{7/2}$ (14.2eV), Ge $3d_{5/2}$ (29.2eV) and Si $2p_{3/2}$ (99.4eV) to obtain similar kinetic energy photoelectrons hence similar probing depth. To account for the change in photon flux as a function of X-ray energy, the Si and Ge signal intensities are normalized with respect to the Hf $4f_{5/2}$ signal. Details of the technique and experiment can be found in the supplement. Data analysis, peak deconvolution and multi-peak fitting were performed with the IGOR Pro software (WaveMetrics, Inc., v.802). After Shirley background subtraction, PES peaks were fitted using Lorentzian-Gaussian type line-shapes using the known binding

energy positions. The Ge $3d_{5/2}$ peak at a binding energy of 29 eV and $Hf4f_{7/2}$ peak at 17.2eV were used as references to correct the spectral shift due to charging effects[29-30].

RESULTS

Multifrequency C-V measurements of the MOSCAP devices along with device structures are presented in Fig. 2. Inset D_{it} values are the peak interface defect density in the band gap obtained with full interface state model. Control devices with 45 ALD cycles of HfO_2 in Fig. 2a exhibit high accumulation capacitance, (C_{max} = 2.25 μF/cm^2) along with high depletion capacitance indicating a high density of interface traps ($D_{it} = 4\times10^{12}$ cm^{-2}eV^{-1}) in comparison to all HfO_2 devices with ozone exposure during (not prior) ALD. Ozone exposure of the SiGe surface for 60 sec prior to HfO_2 deposition doubles the interface trap density to 8×10^{12} cm^{-2}eV^{-1} with negligible change in C_{max} as seen in Fig. 2b. However, ozone insertion after 10 ALD cycles of HfO_2 decreases C_{max} to 2.0 μF/cm^2 along with D_{it} to 2.25×10^{12} cm^{-2}eV^{-1} as shown in Fig. 2c. The 12% reduction in C_{max} is consistent with ozone forming a thicker interfacial layer, and the 45% decrease in D_{it} by changing the location of ozone exposure to 1 nm away from the SiGe surface is significant. This effect was more prominent when the ozone is introduced after 5 cycles of HfO_2 on SiGe which induces a 55% reduction in D_{it} along with 20% decrease in C_{max} (Fig. 2d). Furthermore, when ozone is evenly dispersed into HfO_2 by dosing after every 5 cycles, there is a 63% decrease in D_{it} to $1.5\text{x}10^{12}$ cm^{-2}eV^{-1} compared to the control sample as shown in Fig. 2e. This dispersion of ozone pulses across the HfO_2 reduces D_{it} by 17% in comparison to a single 60 sec ozone pulse as shown in Fig. 2d. Instead of ozone, when water of identical pulse length is dosed for 60 sec after 5 cycles of HfO_2 as shown in Fig 2f, the interface deteriorates and D_{it} increases 15% compared to the control sample indicating that even common reactant species diffusing through gate oxide to the interface during ALD. The impact of ozone exposure during HfO_2 ALD is consistent with ozone dosing several

nanometers from the SiGe still influencing interface trap density and, therefore, HfO_2 ALD being more complex than a true layer-by-layer process.

To elucidate the D_{it} reduction mechanism at the SiGe/HfO_2 interface by ozone exposure into HfO_2, several HfO_2 only and HfO_2-Al_2O_3 hetero gate oxides with ozone exposures are compared. A control Ni/45 cycles of HfO_2 + 5 cycles of Al_2O_3/SiGe device with 1.75 μF/cm^2 and D_{it} of 3.3x10^{12} cm^{-2}eV^{-1} is shown in Fig. 2g. In comparison to the 45 ALD cycles of HfO_2 only control device in Fig. 2a, the control hetero oxide bilayer device exhibits a 18% decrease in D_{it} to 3.3×10^{12} cm^{-2}eV^{-1} consistent with oxygen scavenging by the TMA precursor[5], and a 23% decrease in C_{max} due to increase in total oxide thickness along with the lower dielectric constant of Al_2O_3 in comparison to HfO_2. In comparison to the bilayer control sample in Fig. 2g, the ozone exposed bilayer device in Fig. 2h exhibits only a 25% decrease in D_{it} with negligible change in C_{max}. It is hypothesized that ALD of the bottom Al_2O_3 layer induces GeO_x decomposition to Ge by oxygen scavenging; in addition, the bottom Al_2O_3 may reduce both O_3 and GeO_x diffusion, but this is likely to be a minor effect since as shown below ozone is very effective in reducing D_{it} for Al_2O_3 gate oxides. In sum, the ozone dosing has a modest effect on bilayer HfO_2-Al_2O_3 oxides consistent with the interfacial GeO_x already being at low concentration due to Al_2O_3 deposition[5], and this more modest effect of ozone on bilayer HfO_2-Al_2O_3 samples is consistent with both ozone and TMA dosing reducing interfacial GeO_x but using different chemical processes.

To study the decrease in trap density at the Al_2O_3/SiGe interface by ozone insertion, a set of samples with only Al_2O_3 gate oxide with and without ozone insertion was fabricated (Fig. 2k – o). The control 45 cycles of Al_2O_3 devices have a C_{max} of 1.12 μF/cm^2 and 1.26×10^{12} cm^{-2}eV^{-1} as shown in Fig. 2k. In comparison to control HfO_2 in Fig. 2a and control hetero Al_2O_3 – HfO_2 devices in Fig. 2f, Al_2O_3 only devices exhibit a 70% and 60% lower interface trap density respectively consistent with oxygen scavenging by TMA exposure during Al_2O_3 growth[5]. For ozone insertion into Al_2O_3 after 5 ALD cycles of Al_2O_3 on SiGe as shown in Fig. 2l, the depletion capacitance almost disappears consistent with a 75%

decrease in D_{it} to 0.32×10^{12} $cm^{-2}eV^{-1}$ along with a small decrease in accumulation capacitance in comparison to the control device in Fig. 2k. Conversely, when SiGe is exposed to ozone prior to Al_2O_3 growth, the D_{it} increases significantly without (Fig. 2m) and with sulfur treatment (Fig. 2n) prior to Al_2O_3 growth. The sulfur passivated surface showed lower D_{it} consistent with sulfur reducing GeO_x[17]. The 75% decrease in D_{it} for ozone dosing into Al_2O_3/SiGe devices is consistent with both ozone and TMA dosing reducing interfacial GeO_x but using different yet complementary chemical processes. The TMA reduces GeO_x by gettering the oxygen from $SiGeO_x$ interface to form Al_2O_3 throughout the entire ALD process[5], and it is hypothesized that the ozone promotes GeO_x out diffusion and eventually sublimation to form a Si rich interface. Therefore, two distinct processes take place when ozone is inserted during Al_2O_3 ALD: 1) D_{it} reduction with ozone and 2) oxygen scavenging with remote oxide (TMA) gettering. To confirm the importance of remote gettering and its synergy with ozone dosing for even HfO_2 based gate oxides, both a top Al_2O_3 layer was grown on HfO_2 (Fig 2i) as well as a traditional Al gettering gate (Fig 2j). Compared to an ozone dosed HfO_2-Al_2O_3/SiGe bilayer device (Fig 2h), the ozone dosed Al_2O_3-HfO_2-Al_2O_3/SiGe tri-layer device (fig 2i) exhibits a 44% decrease in D_{it}. This is consistent with remote oxygen scavenging by Al_2O_3 ALD grown on top of HfO_2 which is shown to be an effective method for IL modification for D_{it} reduction even 4 nm from SiGe surface[5].

In the second remote scavenging example, a remote gettering gate Al metal is employed which is separated from the gate oxide with a thin Ni layer as shown in Fig. 2j. This sample was also exposed to additional intentional water exposure after 5 cycles of HfO_2 to deteriorate and increase interface defects. In comparison to the control sample in Fig. 2f, the device with remote Al gettering gate exhibits a 60% decrease in D_{it} with negligible decrease in C_{max}. The data is consistent with the remote gettering by Al metal or a top surface Al_2O_3 ALD layer reducing the D_{it} by a mechanism which is independent of the D_{it} reduction by ozone or increase by H_2O insertion during gate oxide ALD.

Interface defect distributions across the band gap for selected devices calculated with the full interface state model are shown in Fig. 3a. Ozone insertion into HfO_2 only and Al_2O_3 only samples reduce interface traps charges almost uniformly across the bandgap; the integrated D_{it} across the bandgap exhibit 65% and 82% decreases, respectively. In addition, ozone insertion into devices reduces the leakage current consistent with thicker IL formation with ozone dosing as shown in Fig. 3b. Al_2O_3 sample (Fig 2l) had exceptionally low D_{it} because two complementary mechanisms of D_{it} reduction are active: 1) D_{it} reduction with ozone exposure and 2) D_{it} decrease with remote oxygen scavenging via top surface Al_2O_3 ALD. In contrast, for the HfO_2 only device exposed to ozone in Fig. 2, there is only a single D_{it} reduction mechanism.

The interlayer and oxide thicknesses of the selected devices are determined from STEM-HAADF and STEM-BF recorded simultaneously from the MOSCAP device structure in Si <110> projection as shown in Fig. 4. The control Al_2O_3 device in Fig. 4a&f had a darker (HAADF)/brighter (BF) IL region of 0.4 nm along with a 4.9 nm gate oxide thickness indicated with black and white arrows in the images. Furthermore, these assignments are confirmed by compositional analysis. Insertion of ozone into Al_2O_3 forms an IL of similar thickness ~0.2 nm and increases gate oxide thickness to 5.5 nm as shown in Fig. 4b&g. In contrast, insertion of ozone into HfO_2 increases the IL thickness from 0.9 nm to 1.1 nm and increases the gate oxide thickness from 4.2 nm to 4.4 nm as shown in Fig. 2 c&h vs 2d&i respectively. Both results are consistent with the decrease in C_{ox} with ozone insertion into Al_2O_3 (Fig 2k vs 2l) and into HfO_2 (Fig 2a vs 2d); however, the mechanism of D_{it} reduction necessitates the compositional analysis to elucidate the differences in ozone induced reduction/growth with Al_2O_3 vs HfO_2.

STEM-EELS compositional analysis of the selected devices along with associated structures are shown in Fig. 5. STEM-HAADF and BF intensity profiles correlated with EELS analysis are also shown. Note that these STEM images are a representation of similar areas where EELS analyses were performed but are

not taken simultaneously with EELS due to experimental restrains. A multiple linear least square (MLLS) fitting [24] is employed to resolve Al, Hf and Si edges and spectroscopic overlay issues. The IL regions are shaded blue and located between the half maximum of oxygen and the half maximum of Hf. For the Al_2O_3 sample, since there is electron beam induced damage seen in the middle of oxide, the half maximum of the Al is defined by extrapolation of max peak point for the Al signal which is estimated to be 75 (a.u.). The blue IL boundaries are confirmed by correlating the EELS with the corresponding STEM HAADF-BF contrast intensity profiles. The Si - Ge composition in IL is denoted with black and pink arrows respectively; the arrows points to the Si and Ge intensity the middle of the interlayer. As shown in the control HfO_2 device in Fig. 5a, the Hf and O signals have offsets indicating presence of a thick $Si_xGe_xO_x$ IL; the black and pink arrows show high Ge composition in this IL. In contrast, the control Al_2O_3 device in Fig. 5b has a thinner interlayer as documented by the Al and O signals decaying in similar positions. The Al_2O_3 IL has only a small Ge signal (pink) indicating Si rich IL formation. Note that the EELS data indicates a significant Al component in the Al_2O_3/SiGe interlayer, indicating that the IL may be $AlSiO_x$.

The ozone bilayer HfO_2 device shown in Fig. 5c has a larger offset between the Hf and O signals with diminished Ge signal in IL (pink arrow) in comparison to the control device in Fig. 5a, consistent with a thicker Si rich IL region. This ozone bilayer HfO_2 IL has a region which is Hf poor, so it is divided with a dashed line to distinguish regions of $Si_xHf_xO_x$ and $Si_xGe_xO_x$. In addition, the Si peak beyond half max of oxygen extends further into the gate oxide for the ozone bilayer HfO_2 (3 nm from the right edge of the blue region) compared to control HfO_2 (1.5 nm from the right edge of the blue region), consistent with ozone enhancing Si diffusion into HfO_2; the ozone enhanced diffusion of Si is also confirmed by PES data below. Last, for ozone bilayer (Fig 5c), a slightly increased Ge peak near the SiGe surface is observed, consistent with Ge pile-up in the SiGe layer[31-33]. When ozone is dispersed into HfO_2 as shown in Fig. 5d, the Hf – O offset was increased consistent with $Si_xGe_xO_x$ and $Si_xHf_xO_x$ formation. Similar to bilayer ozone

in Fig 5c, the Si signal in the ozone nanolaminate (Fig 5d) extended further into HfO_2 (3.8 nm from the right edge of the blue region), consistent with ozone enhancing Si diffusion into HfO_2 mostly in the IL region. Therefore, the ozone insertion into HfO_2 increases the IL thickness along with increasing the SiO_x concentration in the IL and maybe in HfO_2, whereas ozone decreases the IL thickness and does not change the Si diffusion into the gate oxide for Al_2O_3, which is consistent with Al_2O_3 being a better diffusion barrier to both GeO_x and SiO_x than HfO_2[32].

For better illustration of the Si and Ge distributions, raw EELS data for HfO_2 with dispersed ozone (NL device) is shown in a 3D semi-log graph in Fig. 6a. The elemental profiles of the oxide can be seen from the peaks arising after element specific edges due to electron energy loss; for example, Hf M edges at 1662 eV and the O K edge at 532 eV. The black arrow indicates the SiGe/HfO_2 interface region. Tracing the Si and Ge signal from SiGe into HfO_2 region, Ge decay (green arrow) is observed earlier than the Si decay (orange arrow) consistent with a SiO_x rich IL formation.

Side by side comparison of interface region for HfO_2 devices with raw EELS data after proper background subtraction is shown in Fig. 6b-d. Each color coded and numbered graphical line is an EELS spectrum at a given location on the sample with the corresponding beam spot size indicated on the top right corner of the graphs (note that 5 nm regions parallel to the SiGe surface are averaged). By tracing the Si K edge at 1839 eV and Ge L edges at 1217 eV from SiGe into HfO_2, it is seen at spectrum number 5 that Si and Ge signals decay simultaneously for the control HfO_2 device. In contrast, an earlier Ge decay is seen both in bilayer and NL device at spectrum 5. The only Si peak observed at spectrum line 6 for bilayer and NL devices indicate SiO_x IL formation. The data is consistent with the ozone increasing the Si content of the IL for both the bilayer and NL devices.

It is hypothesized that ozone increases the Si content of the IL by depletion of Ge through oxidation of Ge at the interface which diffuses to the surface of the oxides and then sublimates. To prove the Ge and Si

diffusion hypothesis, PES is employed after full gate oxide deposition since PES has better compositional sensitivity especially for the topmost surface of the sample with low photon energy (see supplement). PES compositional analysis of MOSCAP devices are shown in Fig 7 for Ge (left) and Si (right). The schematic drawings above the graphs are constructed from the STEM-EELS data illustrating the structure and the composition of the samples studied with PES. Metallic Ge^0 at 29eV and Si^0 ($p_{3/2}$) peaks with spin orbit splitting at 99.4eV are seen for all the devices at 1000eV which indicates that the probing depth extends into the SiGe bulk. Broad peaks at 32.6eV and 103.1eV are defined as GeO_2[34] and SiO_2 respectively[29]. Additional analysis and controls are provided in the supplement. It should be noted that in these graphs, the Si and Ge intensities should not be directly compared to each other because the relative sensitivity of the measurement system to the two different elements is not well characterized.

For all the devices, the 150 eV X-ray-energy probed GeO_x shows similar signal intensity for given energy, indicating Ge out diffusion from the SiGe layer through the HfO_2. Conversely, the variation in the Si^{+4} signal intensity among the samples is pronounced. SiO_2 signal is most strong at 150eV consistent with ozone induced Si out diffusion to the surface or the near surface region as the oxide is growing[35-36]. This is consistent with EELS which showing enhancement of Si out diffusion with ozone pulsing. It should be noted that in PES in figure 7 the amount of Ge^{2+} is low compared with Ge^{4+} consistent with the difference in the heats of formation between GeO_2 ($\Delta H° = -580.0$ kJ/mol) and GeO ($\Delta H° = -261.9$ kJ/mol); the greater thermodynamic stability of GeO_2 compared to GeO is consistent with Ge^{4+} dominating the XPS spectra after full device fabrication.

The diminished Si and Ge composition near the oxide top surface in EELS data may seem to be inconsistent with PES data however, as explained in the supplement in detail, this is result of difference in sensitivity and nature of the techniques. It should be emphasized that in PES spectrum the intensity of elements results from the integrated signal from material normal to the SiGe surface while in EELS the integrated signal generated from material parallel to the SiGe surface. It is noted that that at 1000 eV

photon energy, the Si^{+0} is a significant fraction of the Si spectrum in comparison the fraction of Ge^{+0} in the Ge spectrum. Since this effect is only seen at 1000 eV, it must originate Si and Ge at the oxide/SiGe interface. Beam induced decomposition is unlikely since GeO_x is less thermodynamically stable than SiO_x. However, the relative escape probabilities (elastic plus inelastic) of the photoelectrons from Si $2p_{3/2}$ and Ge $3d_{5/2}$ are unknown and likely to differ (see supplement) and, therefore, this region is best studied with STEM-EELS since it gives true composition vs depth. However, the PES data documents the presence of GeO_x and SiO_x on the top surface of the gate oxides or incorporated into the top of the oxide as a germinate or silicate confirming the ozone induced diffusion of GeO_x and SiO_x during ALD.

Discussion and Conclusion

Kinetics of Ge diffusion into gate oxides and GeO desorption from the oxide surface are well-documented[31, 37-39]. Kita et al and others report formation of volatile GeO due to oxidation of Ge at the interface of SiGe (or Ge) which diffuses through the gate oxide and desorbs from the surface as GeO[38, 40-41]. Unlike SiO desorption from surfaces at high temperature (standard sublimation temperature ~780C), sublimation of GeO occurs at low temperature (standard sublimation temperature ~ 400C)[41-42]. GeO_x formation can induce significant Ge consumption from interface[40, 43]. In addition, it has been shown that high pressure oxygen can suppress GeO desorption by forming relatively stable GeO_2 at the oxide-Ge interface which is a common mechanism for the high quality IL on Ge substrates[20-21, 44]; therefore, GeO desorption can be enhanced at low oxidant pressure due transformation from GeO_2 into volatile GeO in an oxygen deficient environment[38, 41]. The standard Gibbs free energy of Si oxidation is higher than that for Ge but for very reactive oxidants, such as atomic O from O_3 dissociation, this difference may be less important. In sum, the Ge out-diffusion into the gate oxide and GeO desorption from the system can be controlled by tuning temperature, oxidant type, and oxidant concentration.

It is hypothesized that interface defect reduction by ozone insertion into HfO_2 gate is primarily induced by enhancement of GeO formation, followed by GeO diffusion through the gate oxide and sublimation of GeO from the gate oxide surface as illustrated in Fig. 8. Ozone from each ozone pulse can diffuse to the SiGe oxide interface and form mobile GeO. This process can deplete Ge from SiGe top layer and form a Si rich IL shown in STEM-EELS. The nature of the Ge diffusion process especially through thin oxide layer is not known. Studies on oxygen vacancy formation and In diffusion in HfO_2 suggest that Ge diffusion would be oxygen vacancy dependent but DFT study is needed for understanding the true mechanism[45-46]. GeO desorption from GeO_2 surface (on Ge substrate) has been shown using thermal desorption spectroscopy (TDS) by Kita et al, since ALD process precludes TDS experiments, the results of Kita et al are used for the proposed mechanism. This process is Ge selective due to the difference in activation energy for GeO desorption and diffusion and the propensity of SiO_x to form a silicate instead of desorbing from gate oxides[42, 47-48]. Preferentially SiO_x formation because of difference in oxidation kinetics of Si versus Ge might also play a role. However, ozone is very active oxidant and each dosing introduces excess of it which is enough to oxidize Ge along with Si on SiGe. Hence, although kinetics of oxidation difference may play a role in these experiments, it cannot be the mechanism for observed results. Reports of the impact of oxygen plasma for Ge and SiGe oxidation (18, 36) suggest that the oxygen radicals (O atoms) can diffuse through the oxide and form GeO_2 at the oxide/SiGe or Ge interface lower defect density. However, plasma oxygen is not preferred since ion or electron bombardment can induce fixed oxide charge traps and may be concern for device reliability**.** Conversely, oxygen molecules (O_2) do not induce any damage but are not reactive as ozone or oxygen radicals; therefore, interface defects reductions is not expected with molecular oxygen exposure during ALD process.

Al_2O_3 only gate oxide growth with ozone insertion on SiGe is very effective for D_{it} reduction because there are two complementary mechanisms are active to reduce D_{it}: 1) ozone selectively depletes Ge from the SiGe surface leaving an Si rich interface, while 2) Al_2O_3 deposition process itself reduces D_{it} driven

by the highly oxygen reactive Al_2O_3 precursor, TMA, and differences in formation enthalpy of GeO_x and SiO_x; the defect reduction occurs by excess TMA diffusing into the oxide and reducing interface defects via oxygen scavenging[5]. Therefore, Al_2O_3 ALD selectively scavenges oxygen from Ge which reduces the IL thickness and forms an ultra-low defect density (D_{it} 3.2×10^{11} $cm^{-2}eV^{-1}$) Al_2O_3 / SiGe interface. Ozone insertion into bilayer HfO_2-Al_2O_3/SiGe is not as effective as ozone insertion into only HfO_2/SiGe devices; this is consistent with the Al_2O_3 in the bilayer already partially decreasing the interfacial GeO_x and reducing the Ge out-diffusion since it is a good diffusion barrier[32]. The TMA diffusion through the gate oxide during ALD is nominally a non-ideality in the ALD mechanism but produces the lowest D_{it} devices.

For HfO_2, the most effective D_{it} reduction with ozone is found when ozone is dispersed into the HfO_2 gate oxide in a nanolaminate structure, consistent with the ozone oxidant continuing to generate interfacial GeO_x and its sublimation during the entire ALD process, thus providing a continuous removal of Ge from the interface. While ALD is usually modeled as a layer by layer process, for gate oxide deposition, the data is more consistent with processes in which the interface continuously evolves during ALD and thus requires continuous defect reduction or post deposition defect reduction process. This continuous defect reduction can be implemented by using an Al_2O_3/HfO_2 nanolaminate to getter oxygen from GeO_x continuously during ALD[5], or by using an ozone-HfO_2 nanolaminate to continuously deplete Ge from the IL by GeO sublimation during ALD, or by using a gettering gate to scavenge oxygen from GeO_x after ALD[18]; however, in all cases these processes depend on facile diffusion of oxidants during or post ALD through the gate oxide. Correlations between experimental results suggest that ALD process itself modifies the oxide-channel interface during the entire ALD process. In essence, the non-ideality of ALD process (even for the Al_2O_3/HfO_2 nanolaminate) is critical for the suppression of electronic defects.

ASSOCIATED CONTENT

Supplementary materials

The supporting information is available free of charge on the ACS Publication website at DOI:

Information about energy-resolved photoelectron spectroscopy (PES) setup and PES spectrum for Si, Ge, Hf, O at various energies.

ACKNOWLEDGEMENTS: Larry Grissom, Sean Parks of the Nano3 clean room and Jian-Guo Zheng of UC Irvine Materials Research Institute (STEM-EDS-EELS were conducted) are acknowledged for great technical support. Vincent Hou from TSMC is appreciated for the discussions on EELS data analysis. This work was funded by TSMC and performed in part at the San Diego Nanotechnology Infrastructure (SDNI) of UCSD, a member of the National Nanotechnology Coordinated Infrastructure, which is supported by the National Science Foundation (Grant ECCS-1542148). This research used resources of the Advanced Light Source, which is a DOE Office of Science User Facility under contract no. DE-AC02-05CH11231.

References

1. Powell, C. J.; Jablonski, A., Dependence of calculated electron effective attenuation lengths on transport mean free paths obtained from two atomic potentials. *Surface and Interface Analysis* **2006,** *38* (10), 1348-1356.
2. Maune, B. M.; Borselli, M. G.; Huang, B.; Ladd, T. D.; Deelman, P. W.; Holabird, K. S.; Kiselev, A. A.; Alvarado-Rodriguez, I.; Ross, R. S.; Schmitz, A. E.; Sokolich, M.; Watson, C. A.; Gyure, M. F.; Hunter, A. T., Coherent singlet-triplet oscillations in a silicon-based double quantum dot. *Nature* **2012,** *481*, 344.
3. Xiao, M.; House, M. G.; Jiang, H. W., Measurement of the Spin Relaxation Time of Single Electrons in a Silicon Metal-Oxide-Semiconductor-Based Quantum Dot. *Physical Review Letters* **2010,** *104* (9), 096801.
4. Coppersmith, S. N.; Lagally, M. G.; Celler, G.; Friesen, M.; McGuire, L. M.; Slinker, K. A.; Goswami, S.; Savage, D. E.; Roberts, M. M.; Klein, L. J.; Eriksson, M. A.; Coppersmith, S. N.; Lagally, M. G.; Celler, G.; Friesen, M.; McGuire, L. M.; Slinker, K. A.; Goswami, S.; Savage, D. E.; Roberts, M. M.; Klein, L. J.; Eriksson, M. A. In *SiGe: Materials and Devices for Quantum Computing?*, 2006 International SiGe Technology and Device Meeting, 15-17 May 2006; 2006; pp 1-1.
5. Kavrik, M. S.; Ercius, P.; Cheung, J.; Tang, K.; Wang, Q.; Fruhberger, B.; Kim, M.; Taur, Y.; McIntyre, P. C.; Kummel, A. C., Engineering High-k/SiGe Interface with ALD Oxide for Selective GeOx Reduction. *ACS Applied Materials & Interfaces* **2019,** *11* (16), 15111-15121.

6. Choi, S.; Tan, S. H.; Li, Z.; Kim, Y.; Choi, C.; Chen, P.-Y.; Yeon, H.; Yu, S.; Kim, J., SiGe epitaxial memory for neuromorphic computing with reproducible high performance based on engineered dislocations. *Nature Materials* **2018,** *17* (4), 335-340.
7. Lu, D., Silicon Germanium FinFET Device Physics, Process Integration and Modeling Considerations. *ECS Transactions* **2014,** *64* (6), 337-345.
8. Höck, G.; Kohn, E.; Rosenblad, C.; Känel, H. v.; Herzog, H.-J.; König, U., High hole mobility in Si0.17Ge0.83 channel metal–oxide–semiconductor field-effect transistors grown by plasma-enhanced chemical vapor deposition. *Applied Physics Letters* **2000,** *76* (26), 3920-3922.
9. Ismail, K.; Chu, J. O.; Meyerson, B. S., High hole mobility in SiGe alloys for device applications. *Applied Physics Letters* **1994,** *64* (23), 3124-3126.
10. Hashemi, P.; Kam-Leung, L.; Ando, T.; Balakrishnan, K.; Ott, J. A.; Koswatta, S.; Engelmann, S. U.; Dae-Gyu, P.; Narayanan, V.; Mo, R. T.; Leobandung, E. In *Demonstration of record SiGe transconductance and short-channel current drive in High-Ge-Content SiGe PMOS FinFETs with improved junction and scaled EOT*, 2016 IEEE Symposium on VLSI Technology, 14-16 June 2016; 2016; pp 1-2.
11. Hashemi, P.; Ando, T.; Balakrishnan, K.; Cartier, E.; Lofaro, M.; Ott, J. A.; Bruley, J.; Lee, K.; Koswatta, S.; Dawes, S.; Rozen, J.; Pyzyna, A.; Chan, K.; Engelmann, S. U.; Park, D.; Narayanan, V.; Mo, R. T.; Leobandung, E. In *Replacement high-K/metal-gate High-Ge-content strained SiGe FinFETs with high hole mobility and excellent SS and reliability at aggressive EOT ∼7Å and scaled dimensions down to sub-4nm fin widths*, 2016 IEEE Symposium on VLSI Technology, 14-16 June 2016; 2016; pp 1-2.
12. Zhang, L.; Guo, Y.; Hassan, V. V.; Tang, K.; Foad, M. A.; Woicik, J. C.; Pianetta, P.; Robertson, J.; McIntyre, P. C., Interface Engineering for Atomic Layer Deposited Alumina Gate Dielectric on SiGe Substrates. *ACS Applied Materials & Interfaces* **2016,** *8* (29), 19110-19118.
13. LeGoues, F. K.; Rosenberg, R.; Nguyen, T.; Himpsel, F.; Meyerson, B. S., Oxidation studies of SiGe. *Journal of Applied Physics* **1989,** *65* (4), 1724-1728.
14. Mitard, J.; Witters, L.; Bardon, M. G.; Christie, P.; Franco, J.; Mercha, A.; Magnone, P.; Alioto, M.; Crupi, F.; Ragnarsson, L.; Hikavyy, A.; Vincent, B.; Chiarella, T.; Loo, R.; Tseng, J.; Yamaguchi, S.; Takeoka, S.; Wang, W.; Absil, P.; Hoffmann, T. In *High-mobility 0.85nm-EOT SiGe pFETs: Delivering high performance at scaled VDD*, 2010 International Electron Devices Meeting, 6-8 Dec. 2010; 2010; pp 10.6.1-10.6.4.
15. Sardashti, K.; Hu, K.-T.; Tang, K.; Madisetti, S.; McIntyre, P.; Oktyabrsky, S.; Siddiqui, S.; Sahu, B.; Yoshida, N.; Kachian, J.; Dong, L.; Fruhberger, B.; Kummel, A. C., Nitride passivation of the interface between high-k dielectrics and SiGe. *Applied Physics Letters* **2016,** *108* (1), 011604.
16. Huang, J.; Wu, N.; Zhang, Q.; Zhu, C.; Li, M. F.; Tay, A. A. O.; Cheng, Z.-Y.; Leitz, C. W.; Lochtefeld, A., Surface NH3 anneal on strained Si0.5Ge0.5 for metal-oxide-semiconductor applications with HfO2 as gate dielectric. *Applied Physics Letters* **2006,** *88* (14), 143506.
17. Sardashti, K.; Hu, K.-T.; Tang, K.; Park, S.; Kim, H.; Madisetti, S.; McIntyre, P.; Oktyabrsky, S.; Siddiqui, S.; Sahu, B.; Yoshida, N.; Kachian, J.; Kummel, A., Sulfur Passivation for the Formation of Si-Terminated Al2O3/SiGe(001) Interfaces. *Applied Surface Science* **2016,** *366* (Supplement C), 455-463.
18. Kavrik, M. S.; Thomson, E.; Chagarov, E.; Tang, K.; Ueda, S. T.; Hou, V.; Aoki, T.; Kim, M.; Fruhberger, B.; Taur, Y.; McIntyre, P. C.; Kummel, A. C., Ultralow Defect Density at Sub-0.5 nm HfO2/SiGe Interfaces via Selective Oxygen Scavenging. *ACS Applied Materials & Interfaces* **2018,** *10* (36), 30794-30802.
19. Lee, C. H.; Kim, H.; Jamison, P.; Southwick, R. G.; Mochizuki, S.; Watanabe, K.; Bao, R.; Galatage, R.; Guillaumet, S.; Ando, T.; Pandey, R.; Konar, A.; Lherron, B.; Fronheiser, J.; Siddiqui, S.; Jagannathan, H.; Paruchuri, V. In *Selective GeOx-scavenging from interfacial layer on Si1−xGexchannel for high mobility Si/Si1−xGexCMOS application*, 2016 IEEE Symposium on VLSI Technology, 14-16 June 2016; 2016; pp 1-2.

20. Zhang, R.; Iwasaki, T.; Taoka, N.; Takenaka, M.; Takagi, S. In *High mobility Ge pMOSFETs with ~ 1nm thin EOT using Al2O3/GeOx/Ge gate stacks fabricated by plasma post oxidation*, 2011 Symposium on VLSI Technology - Digest of Technical Papers, 14-16 June 2011; 2011; pp 56-57.
21. Ando, T.; Hashemi, P.; Bruley, J.; Rozen, J.; Ogawa, Y.; Koswatta, S.; Chan, K. K.; Cartier, E. A.; Mo, R.; Narayanan, V., High Mobility High-Ge-Content SiGe PMOSFETs Using Al2O3/HfO2 Stacks with In-Situ O3 Treatment. *IEEE Electron Device Letters* **2017,** *38* (3), 303-305.
22. Chen, H.-P.; Yuan, Y.; Yu, B.; Chang, C.-S.; Wann, C.; Taur, Y., Re-examination of the Extraction of MOS Interface-State Density by C–V Stretchout and Conductance Methods. *Semiconductor Science and Technology* **2013,** *28* (8), 085008.
23. Chen, H. P.; Yuan, Y.; Yu, B.; Ahn, J.; McIntyre, P. C.; Asbeck, P. M.; Rodwell, M. J. W.; Taur, Y., Interface-State Modeling of Al2O3 InGaAs MOS From Depletion to Inversion. *IEEE Transactions on Electron Devices* **2012,** *59* (9), 2383-2389.
24. Leapman, R. D.; Swyt, C. R., Separation of Overlapping Core Edges in Electron Energy Loss Spectra by Multiple-Least-Squares Fitting. *Ultramicroscopy* **1988,** *26* (4), 393-403.
25. Satake, T.; Yamamoto, M.; Natio, S.; Mabuchi, M.; Kaneda, A.; Kurahashi, M.; Hashino, T., Auger electron, electron energy loss, secondary electron emission and secondary ion mass spectroscopic studies on the oxidation of hafnium at room temperature. *Journal of the Chemical Society, Faraday Transactions* **1993,** *89* (19), 3611-3618.
26. Iacona, F.; Kelly, R.; Marletta, G., X-ray photoelectron spectroscopy study of bombardment-induced compositional changes in ZrO2, SiO2, and ZrSiO4. *Journal of Vacuum Science & Technology A* **1999,** *17* (5), 2771-2778.
27. Merzlikin, S. V.; Tolkachev, N. N.; Strunskus, T.; Witte, G.; Glogowski, T.; Wöll, C.; Grünert, W., Resolving the depth coordinate in photoelectron spectroscopy – Comparison of excitation energy variation vs. angular-resolved XPS for the analysis of a self-assembled monolayer model system. *Surface Science* **2008,** *602* (3), 755-767.
28. Girard-Lauriault, P.-L.; Gross, T.; Lippitz, A.; Unger, W. E. S., Chemical and Elemental Depth Profiling of Very Thin Organic Layers by Constant Kinetic Energy XPS: A New Synchrotron XPS Analysis Strategy. *Analytical Chemistry* **2012,** *84* (14), 5984-5991.
29. Schmeisser, D.; Schnell, R. D.; Bogen, A.; Himpsel, F. J.; Rieger, D.; Landgren, G.; Morar, J. F., Surface oxidation states of germanium. *Surface Science* **1986,** *172* (2), 455-465.
30. Morant, C.; Galán, L.; Sanz, J. M., An XPS study of the initial stages of oxidation of hafnium. *Surface and Interface Analysis* **1990,** *16* (1-12), 304-308.
31. Lu, N.; Bai, W.; Ramirez, A.; Mouli, C.; Ritenour, A.; Lee, M. L.; Antoniadis, D.; Kwong, D. L., Ge Diffusion in Ge Metal Oxide Semiconductor with Chemical Vapor Deposition HfO2 Dielectric. *Applied Physics Letters* **2005,** *87* (5), 051922.
32. Ogawa, S.; Asahara, R.; Minoura, Y.; Sako, H.; Kawasaki, N.; Yamada, I.; Miyamoto, T.; Hosoi, T.; Shimura, T.; Watanabe, H., Insights into Thermal Diffusion of Germanium and Oxygen Atoms in HfO2/GeO2/Ge Gate Stacks and Their Suppressed Reaction with Atomically thin AlOx Interlayers. *Journal of Applied Physics* **2015,** *118* (23), 235704.
33. Long, E.; Galeckas, A.; Kuznetsov, A. Y., Ge concentrations in pile-up layers of sub-100-nm SiGe films for nano-structuring by thermal oxidation. *Journal of Vacuum Science & Technology B* **2012,** *30* (4), 041212.
34. Prabhakaran, K.; Ogino, T., Oxidation of Ge(100) and Ge(111) surfaces: an UPS and XPS study. *Surface Science* **1995,** *325* (3), 263-271.
35. Prabhakaran, K.; Ogino, T.; Scimeca, T.; Watanabe, Y.; Oshima, M., Bonding partner change reaction in oxidation of Ge on Si(001): Observation of two step formation of SiO2. *Applied Physics Letters* **1994,** *64* (14), 1839-1841.

36. Prabhakaran, K.; Nishioka, T.; Sumitomo, K.; Kobayashi, Y.; Ogino, T., In situ oxidation of a thin layer of Ge on Si(001): Observation of GeO to SiO2 transition. *Applied Physics Letters* **1993,** *62* (8), 864-866.
37. Hosoi, T.; Hideshima, I.; Tanaka, R.; Minoura, Y.; Yoshigoe, A.; Teraoka, Y.; Shimura, T.; Watanabe, H., Ge diffusion and bonding state change in metal/high-k/Ge gate stacks and its impact on electrical properties. *Microelectronic Engineering* **2013,** *109* (Supplement C), 137-141.
38. Kita, K.; Wang, S. K.; Yoshida, M.; Lee, C. H.; Nagashio, K.; Nishimura, T.; Toriumi, A. In *Comprehensive study of GeO2 oxidation, GeO desorption and GeO2 metal interaction -understanding of Ge processing kinetics for perfect interface control*, 2009 IEEE International Electron Devices Meeting (IEDM), 7-9 Dec. 2009; 2009; pp 1-4.
39. Oniki, Y.; Koumo, H.; Iwazaki, Y.; Ueno, T., Evaluation of GeO desorption behavior in the metal/GeO2/Ge structure and its improvement of the electrical characteristics. *Journal of Applied Physics* **2010,** *107* (12), 124113.
40. Oh, J.; Campbell, J. C., Thermal desorption of Ge native oxides and the loss of Ge from the surface. *Journal of Electronic Materials* **2004,** *33* (4), 364-367.
41. Hansen, D. A.; Hudson, J. B., The adsorption kinetics of molecular oxygen and the desorption kinetics of GeO on Ge(100). *Surface Science* **1993,** *292* (1), 17-32.
42. Prabhakaran, K.; Maeda, F.; Watanabe, Y.; Ogino, T., Distinctly different thermal decomposition pathways of ultrathin oxide layer on Ge and Si surfaces. *Applied Physics Letters* **2000,** *76* (16), 2244-2246.
43. Wang, S. K.; Kita, K.; Lee, C. H.; Tabata, T.; Nishimura, T.; Nagashio, K.; Toriumi, A., Desorption kinetics of GeO from GeO2/Ge structure. *Journal of Applied Physics* **2010,** *108* (5), 054104.
44. Mukhopadhyay, M.; Ray, S. K.; Maiti, C. K.; Nayak, D. K.; Shiraki, Y., Electrical properties of oxides grown on strained SiGe layer at low temperatures in a microwave oxygen plasma. *Applied Physics Letters* **1994,** *65* (7), 895-897.
45. Ferrari, S.; Fanciulli, M., Diffusion Reaction of Oxygen in HfO2/SiO2/Si Stacks. *The Journal of Physical Chemistry B* **2006,** *110* (30), 14905-14910.
46. Hu, Y.; Wang, C.; Dong, H.; Wallace, R. M.; Cho, K.; Wang, W.-H.; Wang, W., Origin of Indium Diffusion in High-k Oxide HfO2. *ACS Applied Materials & Interfaces* **2016,** *8* (11), 7595-7600.
47. NIST, NIST Chemistry WebBook, SRD 69. **2017**.
48. Uematsu, M., Self-diffusion and impurity diffusion in silicon dioxide. *Journal of Phase Equilibria and Diffusion* **2005,** *26* (5), 547-554.

Figure 1. Schematic Diagram of MOSCAP Structure and Photon Energy Dependent PES Experiment Geometry. MOSCAP device with 5nm HfO_2 gate oxide and Ni metal gates are displayed. X-ray photons from the synchrotron source is focused on sample with a beam spot of 40 x 40 m on the HfO_2 surface between the Ni gate metals of the MOSCAP devices. Emission angle: incident photon angle to the sample normal is 54.75°. X-ray penetration depth is much deeper than the HfO_2 and SiGe layer thickness; however, the inelastic mean free path (λ) (IMFP) of the photoelectrons emitted by the elements is limited by the kinetic energy of the photo electrons. By using x-ray energy of 150eV, 500eV and 1000eV, the MFP of photoelectrons is varied, and deeper composition profiles obtained. Since the Si, Hf and Ge binding energies are similar, the IMFP of photoelectrons are similar which provides information from same depth. It should be noted that photoelectrons can be scattered elastically with longer mean free path such as photoelectrons at ~1keV in HfO_2 is ~6 nm ADDIN EN.CITE <EndNote><Cite><Author>Powell</Author><Year>2006</Year><RecNum>110</RecNum><DisplayText><style face="superscript">1</style></DisplayText><record><rec-number>110</rec-number><foreign-keys><key app="EN" db-id="v95vdff029zfx0edd5vptptst5swv5zfae0z" timestamp="1546107054">110</key></foreign-keys><ref-type name="Journal Article">17</ref-type><contributors><authors><author>Powell, C. J.</author><author>Jablonski, A.</author></authors></contributors><titles><title>Dependence of calculated electron effective attenuation lengths on transport mean free paths obtained from two atomic potentials</title><secondary-title>Surface and Interface Analysis</secondary-title></titles><periodical><full-title>Surface and Interface Analysis</full-title></periodical><pages>1348-1356</pages><volume>38</volume><number>10</number><

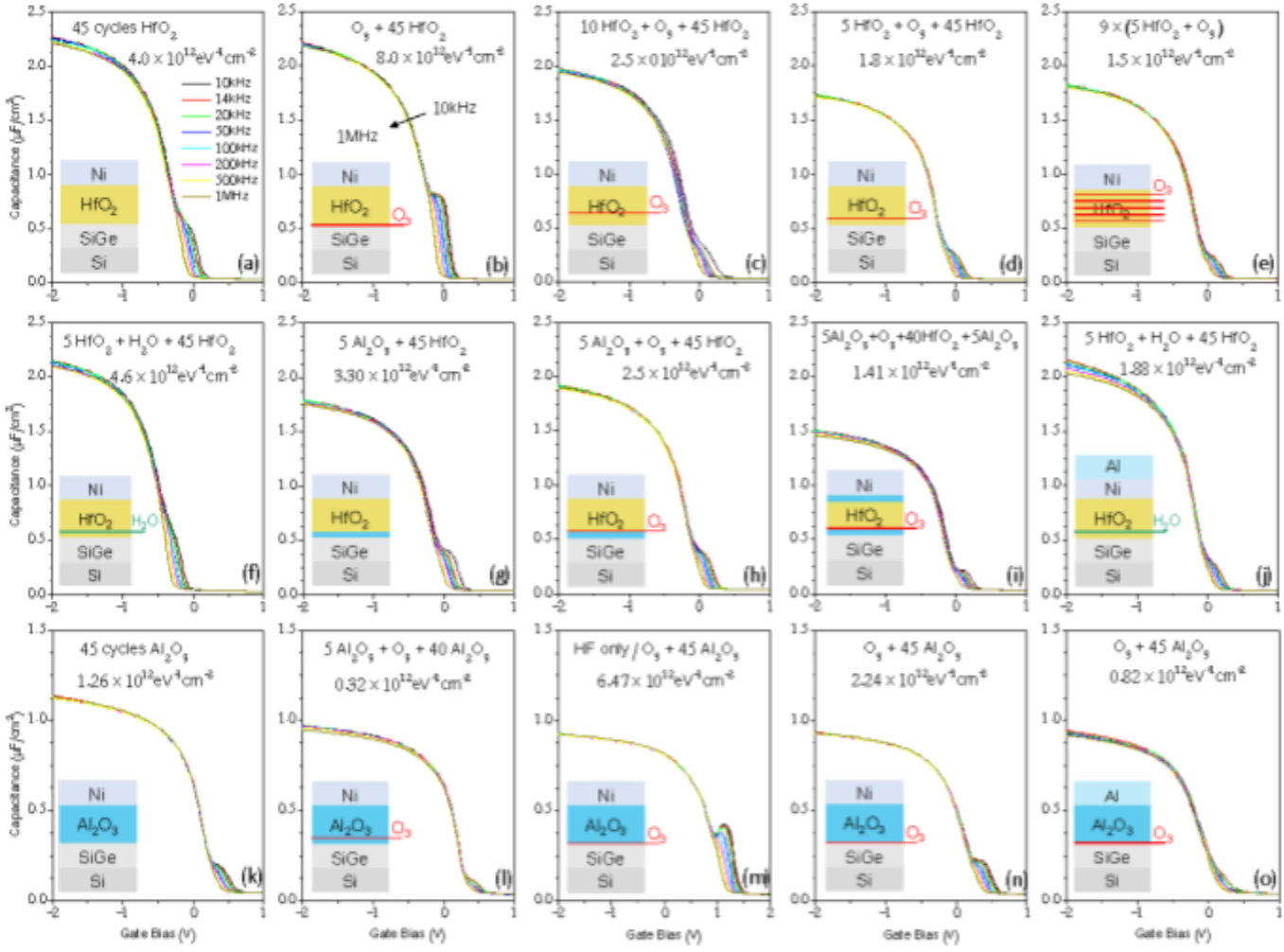

Fig 2: Multi frequency C-V graphs of HfO_2/SiGe MOSCAPs. Inset drawings illustrate device structure along with the description above for a given graph. Except the device in m, all devices are treated with sulfur passivation prior to ALD oxide growth after native oxide removal. (a) SiGe/45 cycles of HfO_2/Ni; (b) single 60 sec ozone pulse prior to HfO_2 ALD (SiGe/60 s O_3 dose /45 cycles of HfO_2/Ni); (c) single 60 sec ozone pulse after 10 HfO_2 ALD cycles (SiGe/ 10 HfO_2 /60 s O_3 /35 HfO_2/Ni); (d) single 60 sec ozone pulse after 5 HfO_2 ALD cycles (SiGe/ 5 HfO_2 /60 s O_3 /35 HfO_2/Ni); (e) nanolaminate with 5 seconds of ozone after each 5 HfO_2 ALD cycles SiGe/ 9×(5 HfO_2 + 5s O_3) /Ni ; (f) 5 sec H_2O pulse after 5 cycles of HfO_2 oxide deposition (SiGe/ 5 HfO_2 / 5s H_2O / 45 HfO_2 /Ni); (g) bilayer device (SiGe/ 5 Al_2O_3 / 45 HfO_2 /Ni); (h) 60 sec ozone pulse between Al_2O_3 and HfO_2 ALD cycles (SiGe/ 5 Al_2O_3 / 60 s O_3 / 45 HfO_2 /Ni); (i) 60 sec ozone pulse between Al_2O_3 and HfO_2 ALD cycles in tri-layer structure (SiGe/ 5 Al_2O_3 / 60 s O_3 / 45 HfO_2 / 5 Al_2O_3 /Ni); (j) 5 sec H_2O pulse after 5 cycles of HfO_2 oxide deposition (SiGe/ 5s H_2O / 5 H_2O / 40 HfO_2 /Ni/Al); (k) Control Al_2O_3 device (SiGe/ 45 Al_2O_3 / Ni); (l) single 60 sec ozone pulse after 5 Al_2O_3 ALD cycles (SiGe/ 5 Al_2O_3 /60 s O_3 /35 Al_2O_3 /Ni); (m) single 60 sec ozone pulse prior to Al_2O_3 ALD, (SiGe / 60 s O_3 dose /45 cycles of Al_2O_3 /Ni), this device has only

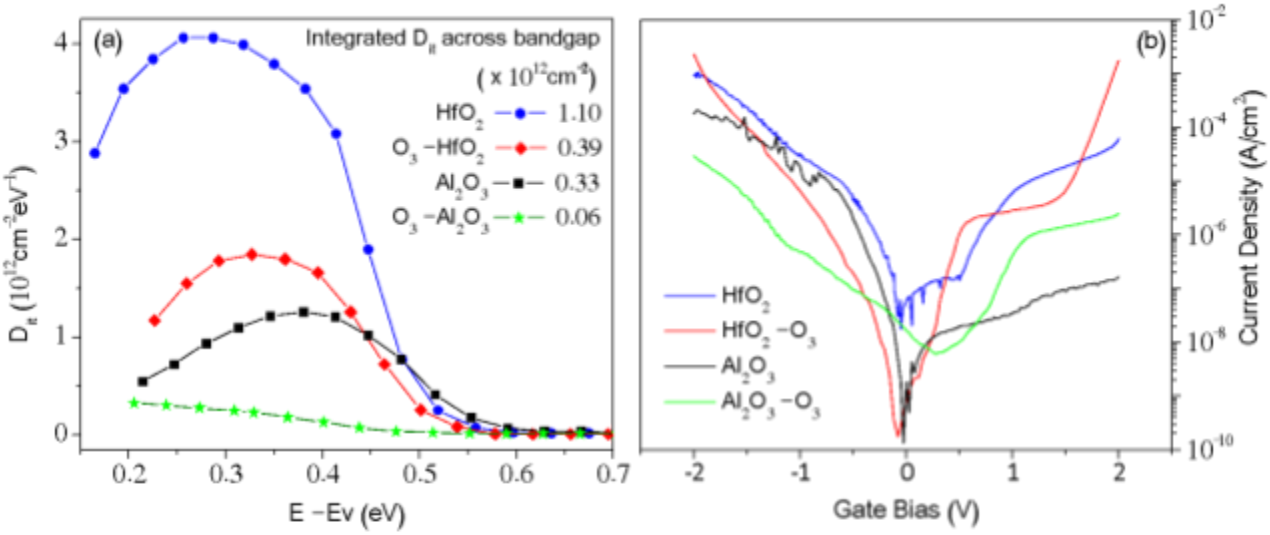

Fig 3: Defect Density Distribution and Leakage Current Comparison: (a) Interface defect density distribution of MOSCAPs across the band gap. b) Leakage current density across the gate oxide for the devices. The full interface state model is used to extract the defect density across the bandgap. In comparison to the 45 cycles HfO_2 control device with 4×10^{12} $eV^{-1}cm^{-2}$ (peak D_{it}), ozone pulsed bilayer devices with 5 ALD cycles of HfO_2 /60 sec O_3/40 ALD cycles of HfO_2 shows 1.8×10^{12} $eV^{-1}cm^{-2}$. Defect density is significantly lower for Al_2O_3 control devices in comparison to control HfO_2 and decreases further with ozone insertion for 5 Al_2O_3/60 sec O_3/40 ALD cycles of Al_2O_3 which exhibits 0.3×10^{12} $eV^{-1}cm^{-2}$. Inset values indicates total defect density across the band gap and shows more prominent decrease in trap density by ozone insertion. Devices with ozone have lower leakage current in comparison to control devices as indicates in the I-V graph on the right.

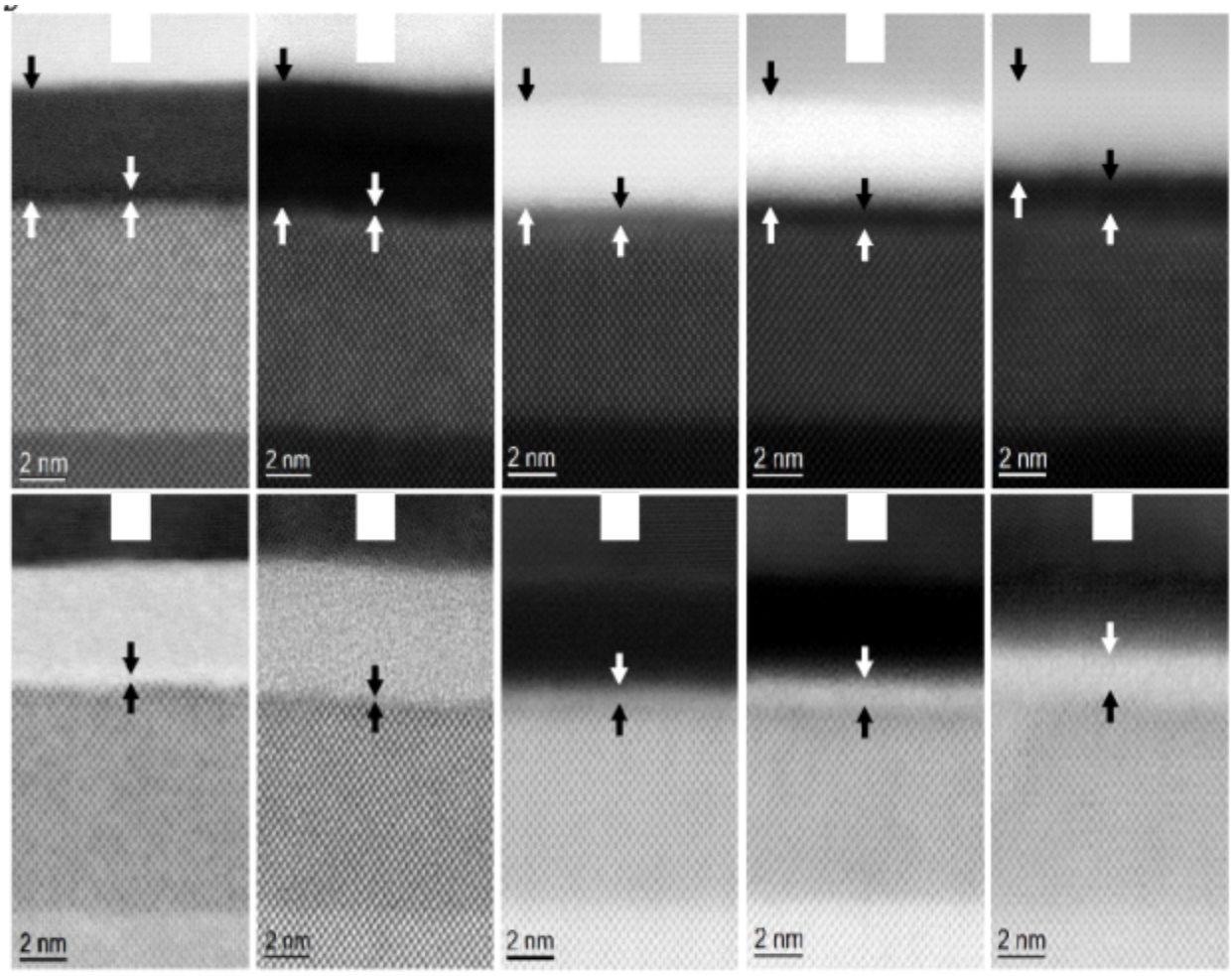

Fig 4. STEM HAADF and BF images of MOSCAPs (a, f) 45 cycles of Al_2O_3; (b, g) 5 cycles of Al_2O_3/60 sec O_3/40 cycles of Al_2O_3 (c, h) control device of 45 cycles HfO_2; (d, i) bilayer device with 5 cycles of HfO_2/60 sec O_3/ 40 cycles of HfO_2/Ni structure; (e, j) nanolaminate with 9 x (5HfO_2 + 5 sec O_3) ALD cycles. In these images, the oxide structures and regions are defined according to z contrast. The interfacial layer between SiGe and oxide are indicated with black and white arrows on corresponding STEM-HAADF and BF images. The control Al_2O_3 device had a 0.4 nm low z interface layer in comparison to < 0.2 nm thick IL in the ozone-Al_2O_3 device. In comparison to control device of HfO_2/SiGe (c&h), bilayer (d&i) and NL (e&j) shows thicker interfaces consistent ozone forming thicker oxide at the interface.

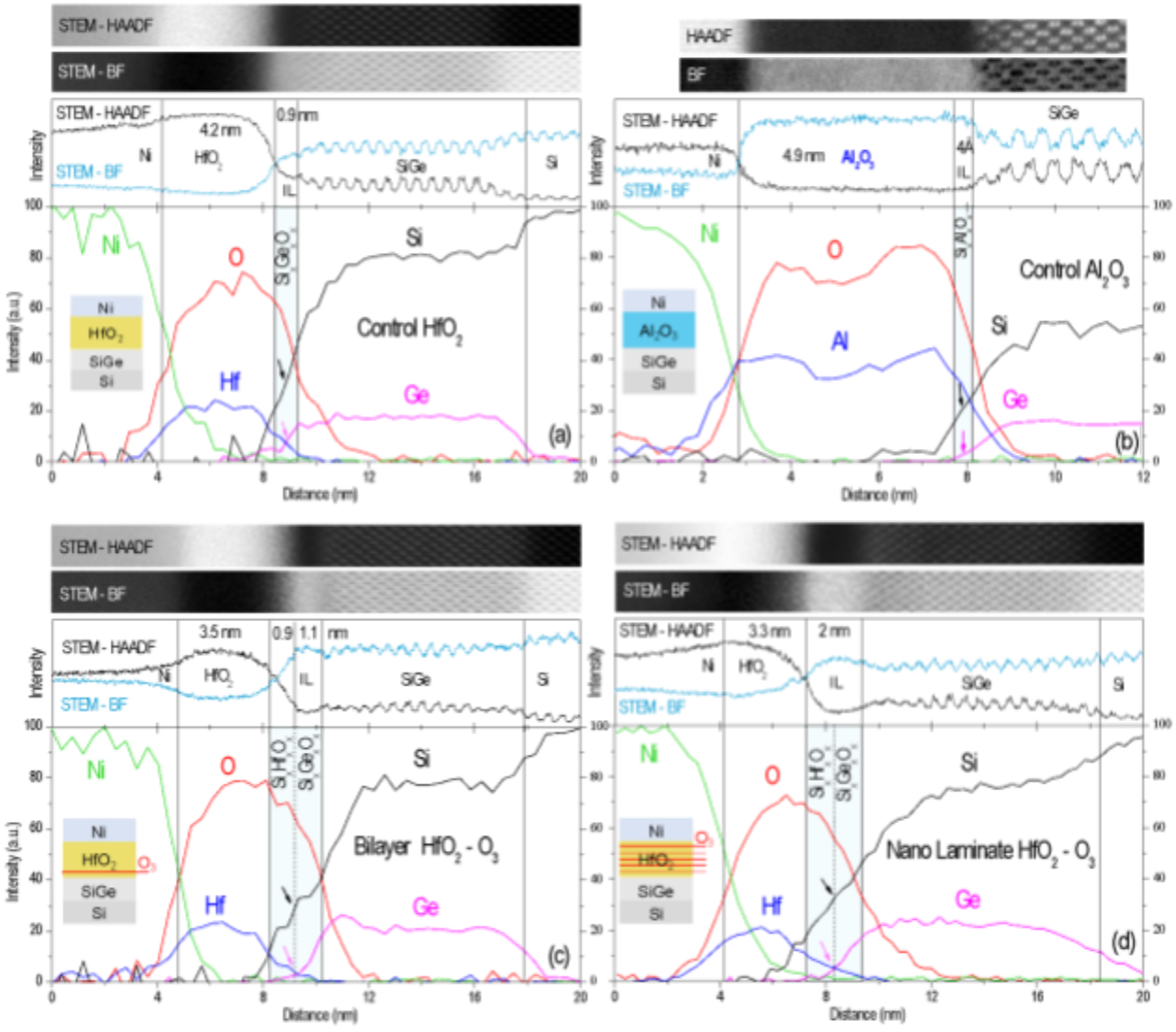

Figure 5. STEM- EELS compositional analysis of MOSCAP devices. (a) 45 cycles of HfO_2 control device; (b) 45 cycles of Al_2O_3 control device (c) bilayer device with 5 ALD cycles of HfO_2 / 60 sec O_3 / 40 ALD cycles of HfO_2 structure; (d) nanolaminate with 9 x (5HfO_2 + 5 sec O_3) ALD cycles devices. The EELS experiment is performed at 200keV. Inset drawings illustrate the corresponding device structure. The graphs above the EELS data indicates the intensity of the STEM – HAADF and BF images. Note that the STEM images are not taken

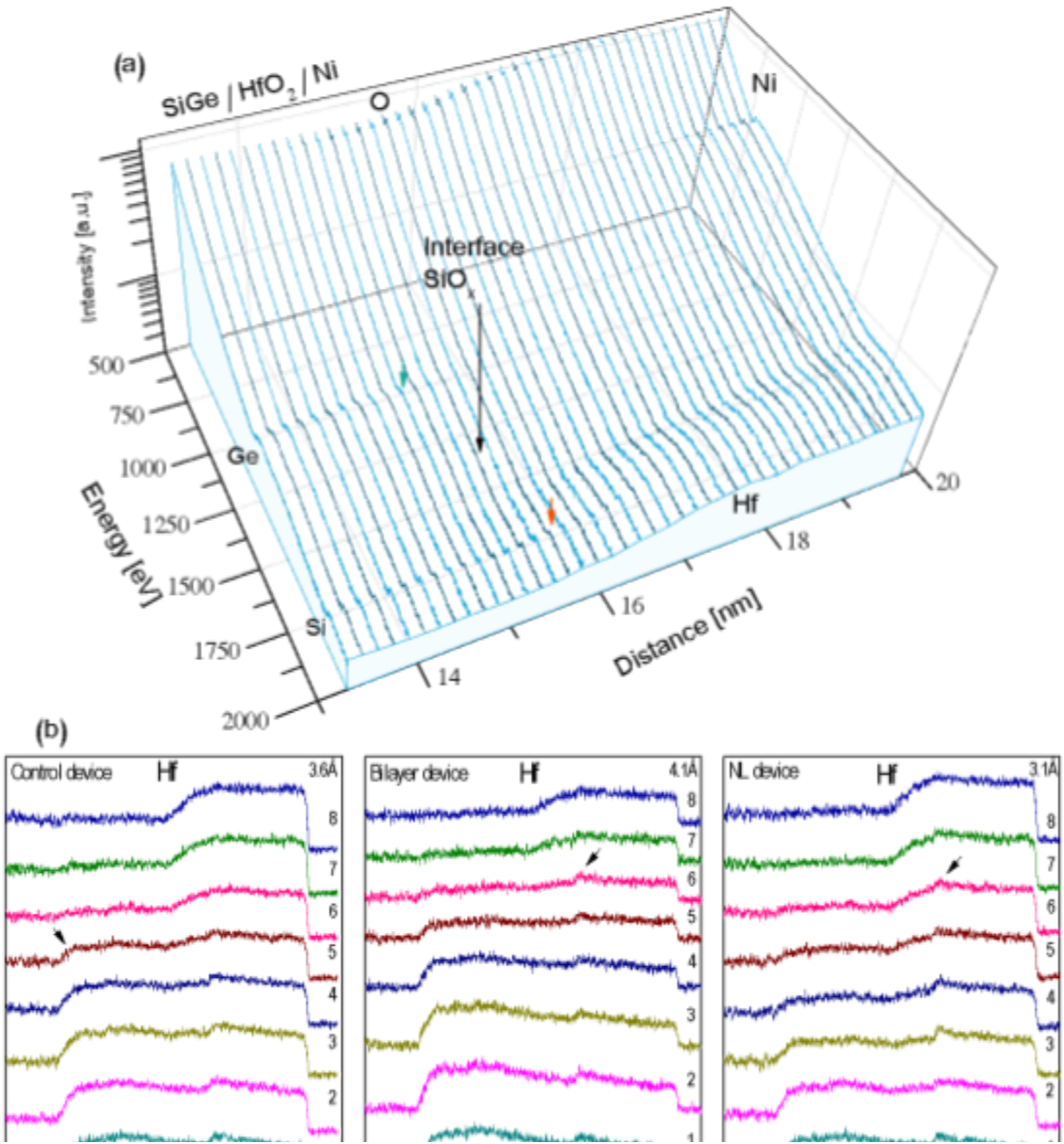
(a)
SiGe / HfO2 / Ni
O
Ni
Interface
SiOx
Ge
Si
Hf
Intensity [a.u.]
Energy [eV]
500
750
1000
1250
1500
1750
2000
14
16
18
20
Distance [nm]
(b)
Control device
Hf
3.6Å
Bilayer device
Hf
4.1Å
NL device
Hf
3.1Å
8
7
6
5
4
3
2
1

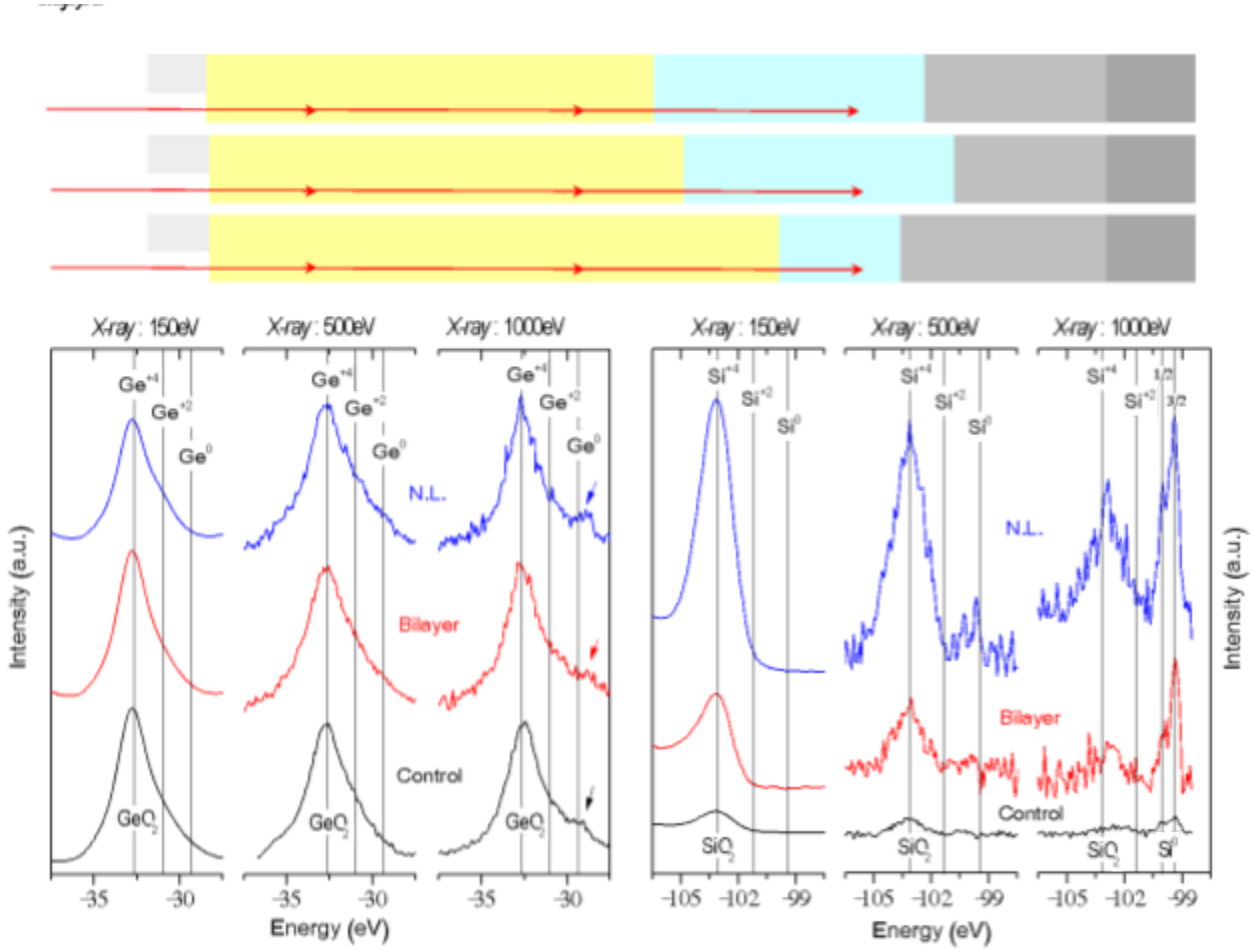
X-ray : 150eV
X-ray : 500eV
X-ray : 1000eV
Ge+4
Ge+2
Ge0
GeO2
N.L.
Bilayer
Control
Intensity (a.u.)
Energy (eV)
-35
-30
X-ray : 150eV
X-ray : 500eV
X-ray : 1000eV
Si+4
Si+2
Si0
SiO2
N.L.
Bilayer
Control
Intensity (a.u.)
Energy (eV)
-105
-102
-99

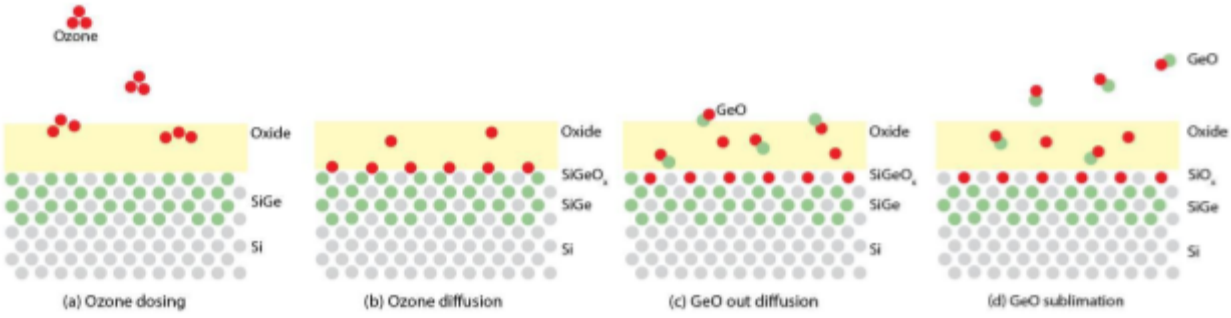

Figure 8. Schematic drawing of interface defect reduction mechanism with ozone insertion into oxide during ALD process. Interface defect reduction mechanism on SiGe with ozone dosing explained in four steps. (a) Ozone diffuses into the gate oxide, (b) ozone dissociates and oxygen bonds to interfacial Si and Ge atoms to form $SiGeO_x$, (c) GeO out diffuses into gate oxide, (d) GeO desorbs from the surface and leaves an SiO_x rich interface behind.

TOC